Short-exposure Turbulent Tilt-phase Frequency Dependence in Passive Imaging

by David H. Tofsted

ARL-TR-6254 **November 2012**

NOTICES

Disclaimers

The findings in this report are not to be construed as an official Department of the Army position unless so designated by other authorized documents.

Citation of manufacturer's or trade names does not constitute an official endorsement or approval of the use thereof.

Destroy this report when it is no longer needed.   Do not return it to the originator.

Army Research Laboratory

White Sands Missile Range, NM 88002-5501

Short-exposure Turbulent Tilt-phase Frequency Dependence in Passive Imaging

David H. Tofsted

Computational and Information Sciences Directorate, ARL

REPORT DOCUMENTATION PAGE

Form Approved
OMB No. 0704-0188

1. REPORT DATE (DD-MM-YYYY)	2. REPORT TYPE	3. DATES COVERED (From - To)
November 2012	Final	06 2011-08 2012

4. TITLE AND SUBTITLE	5a. CONTRACT NUMBER
Short-exposure Turbulent Tilt-phase Frequency Dependence in Passive Imaging	
	5b. GRANT NUMBER
	5c. PROGRAM ELEMENT NUMBER
6. AUTHOR(S) David H. Tofsted	5d. PROJECT NUMBER
	5e. TASK NUMBER
	5f. WORK UNIT NUMBER

7. PERFORMING ORGANIZATION NAME(S) AND ADDRESS(ES)	8. PERFORMING ORGANIZATION REPORT NUMBER
U.S. Army Research Laboratory ATTN: RDRL-CIE-D White Sands Missile Range, NM 88002-5501	ARL-TR-6254

9. SPONSORING/MONITORING AGENCY NAME(S) AND ADDRESS(ES)	10. SPONSOR/MONITOR'S ACRONYM(S)
	11. SPONSOR/MONITOR'S REPORT NUMBER(S)

12. DISTRIBUTION/AVAILABILITY STATEMENT

Approved for public release; distribution is unlimited.

14. ABSTRACT

In a previous paper, short-exposure imaging through atmospheric turbulence was shown to include a non-negligible tilt-phase effect. This effect was modeled as a modifying factor, $\exp[A(X,Q)\,\omega^2]$, dependent on a normalized angular frequency, ω, and a function A dependent on non-dimensional turbulence (X) and diffraction (Q) related parameters. The present paper describes a subsequent analysis performed at high $A\omega^2$ values that has revealed an additional moderate ω dependence in A. The new functionality of $A(X,Q,\omega)$ produces diffraction limited behavior at high frequency, but increases the amount of correction of short-exposure turbulence effects at intermediate frequencies. The resulting behavior is parameterized through a new series of analytic expressions.

15. SUBJECT TERMS

Turbulence, imaging, short-exposure

16. SECURITY CLASSIFICATION OF:			17. LIMITATION OF ABSTRACT	18. NUMBER OF PAGES	19a. NAME OF RESPONSIBLE PERSON David H. Tofsted
a. REPORT	b. ABSTRACT	c. THIS PAGE	UU	30	19b. TELEPHONE NUMBER (Include area code) 575-678-3039
Unclassified	Unclassified	Unclassified			

Standard Form 298 (Rev. 8/98)
Prescribed by ANSI Std. Z39.18

Contents

List of Figures

iv

List of Tables

1.   Introduction

In the prequel (*1*) to the present paper the Fried approach to short-exposure imaging through optical turbulence (*2*) was reanalyzed. The subject of that study was the short-exposure modulation transfer function (MTF) that describes the mean behavior of a system acquiring short-exposure images through turbulence. This MTF is commonly described as the product of a system MTF and an atmospheric MTF. In the short-exposure case, the net MTF is expressed using the equation,

$$M_S(\omega) = \frac{4}{\pi} \int d\boldsymbol{u}\, W_1(\boldsymbol{u})\, W_1(\boldsymbol{u} - \boldsymbol{\omega}) \times \exp\left\{ -\frac{[\mathcal{D}_\ell(D\,|\boldsymbol{\omega}|) + \mathcal{D}_\psi(D\,|\boldsymbol{\omega}|)]}{2} \right\}, \tag{1}$$

where $\boldsymbol{u}$ and $\boldsymbol{\omega}$ are normalized two-dimensional vectors. $\boldsymbol{u} = \boldsymbol{x}/D$ is a position vector in a normalized aperture, while $\boldsymbol{\omega}$ is an angular frequency vector of the plane perpendicular to the main axis of propagation. $\omega = |\boldsymbol{\omega}| = \Omega/\Omega_0$, expresses angular frequency relative to $\Omega_0 = D/\lambda$ the maximum angular frequency (cyc/mrad) passed through an aperture of diameter D by radiation of wavelength λ (see, e.g., Goodman (*3*)). W_1 is a normalized aperture function,

$$W_D(\boldsymbol{x}) = \begin{cases} 1, & |\boldsymbol{x}| < D/2; \\ 0, & |\boldsymbol{x}| > D/2 ; \end{cases} \tag{2}$$

and $\mathcal{D}_\ell(D\omega)$ and $\mathcal{D}_\phi(D\omega)$ are amplitude and phase structure functions.

This short-exposure MTF is usually written as the product,

$$M_S(\omega) = M_0(\omega)\, M_{SA}(\omega), \tag{3}$$

where, $M_0(\omega)$ is the system MTF, given by,

$$M_0(\omega) = \frac{4}{\pi} \int d\boldsymbol{u}\, W_1(\boldsymbol{u})\, W_1(\boldsymbol{u} - \boldsymbol{\omega}) = \frac{\left[\cos^{-1}(\omega) - \omega\sqrt{1 - \omega^2} \right]}{\pi/2} W_2(\omega). \tag{4}$$

The key contribution in the former paper involved the retention of a tilt-phase correlation term that produced turbulence and diffraction related effects on the short-exposure correction to the atmospheric MTF. The present paper improves upon this expression by exploring further into the space of a fourth-order integral introduced in the previous analysis. Further investigation into the behavior of this integral has revealed a new dependence.

To describe this new dependency, we first consider Fried's original formulation of the short-exposure atmospheric MTF (SAMTF). According to the standard approach, the SAMTF is itself formed as a correction to the long-exposure atmospheric MTF (LAMTF), which is written,

$$M_{LA}(\omega) = \exp\{-(2.1\,X\,\omega)^{5/3}\}, \tag{5}$$

wherein the factor $X = D/r_o$ represents the ratio of the system entrance pupil diameter to the Fried coherence length (2), which for homogeneous Kolmogorov turbulence may be expressed as,

$$r_o = 2.1 \times 1.437 \left(k^2\,L\,C_n^2\right)^{-3/5}, \tag{6}$$

with $k = 2\pi/\lambda$ the optical wavenumber, L the path length, and C_n^2 [m$^{-2/3}$] the refractive index structure parameter. From the LAMTF, the SAMTF has been expressed as a perturbation,

$$M_{SA}(\omega) = \exp\{-(2.1\,X)^{5/3}\,[\omega^{5/3} - V(Q,X)\,\omega^2]\}, \tag{7}$$

where $V(Q,X)$ was modeled as a constant in Fried's original analysis (denoted as α), taking values of either 1/2 or 1. In the re-analysis of Tofsted (1), $V(Q,X)$ was shown to vary with both X and a diffraction-related parameter $Q = D/P$, where $P = (\lambda\,L)^{1/2}$ is a Fresnel scaling parameter. Together, the X and Q parameters account for turbulence and diffraction influences on V.

The meaning of this short-exposure correction derives from Fried's observation that long-exposure imaging averages over all phase aberrations in the system aperture, but when performing short-exposure imaging the tilt of the incident wave may shift the centroid of a given object point, but would not affect its image clarity. The correction factor, $V(Q,X)\,\omega^2$, removes this tilt effect, which accounts for both a tilt-variance effect and a tilt-phase correlation term,

$$V(Q,X) = N(Q,X) - 1.0433\,G(Q). \tag{8}$$

where $N(Q,X)$ represented the tilt-phase term, and $G(Q)$ represented the diffraction-influenced tilt-variance effect.

$V(Q,X)$ was approximated in the prequel using the analytic form,

$$V(Q,X) \approx A + \frac{B}{10}\,\exp\left[-\frac{(x+1)^3}{3.5}\right], \tag{9}$$

2

where $x = \log_{10}(X)$, and functions A and B were modeled as functions of Q, using a log-variable version, $q = \log_2(Q)$:

$$A = \begin{cases} 0.840 + 0.280\,\Sigma(q_a), & q_a = 0.51\,(q + 1.50); & q \leq -1.50 \\ 0.840 + 0.116\,\Sigma(q_b), & q_b = 1.35\,(q + 1.50); & q \geq -1.50 \end{cases} \tag{10}$$

$$B = 0.805 + 0.265\,\Sigma(q_c), \quad q_c = 1.45\,(q - 0.15), \tag{11}$$

where $\Sigma(z) = [\exp(z) - 1]/[\exp(z) + 1]$ is a sigmoidal function. The behavior of $V(Q, X)$ is plotted in figure 1 which is a reproduction of figure 4 of Tofsted (1).
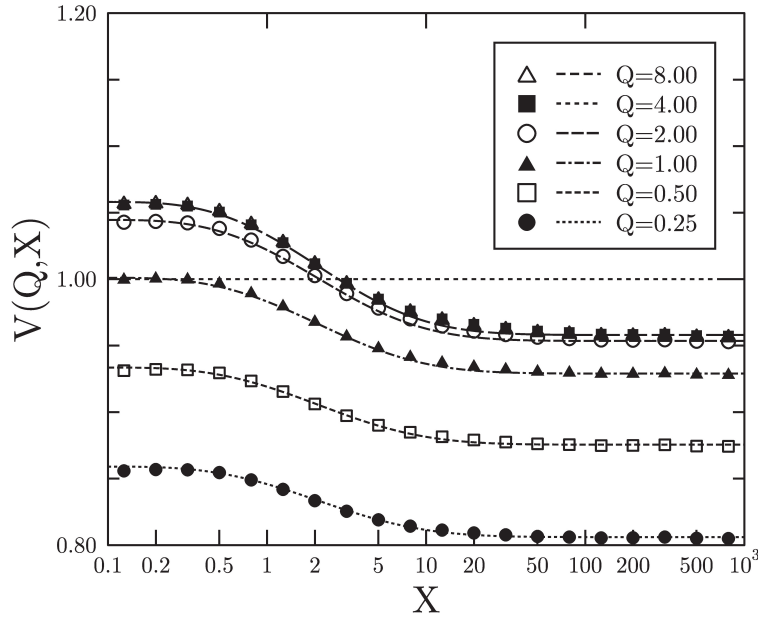
Figure 1. Intercomparison of $V(Q, X)$ results for varying Q as a function of X from the prequel.

Subsequent to the publication of Tofsted (1), questions arose regarding the validity of the $V(Q, X)$ function and the implication that super-resolution results were obtained (4). Review and reinvestigation have confirmed elements of Charnotskii's critique and have led to the current paper.

In the reinvestigation, it was first noted that equation 1 could be formed through a combination of equations 28, 29, and 56 of Tofsted (1), but the structure functions within the exponential are positive definite, representing mean squared quantities. However, if $V(Q, X)$ exceeds unity M_{SA} will exceed unity at high ω, as it does when $X < 2 < Q$ (see figure 1).

The calculation of $V(Q, X)$ primarily relied on evaluation of $N(Q, X)$ based on the model,

$$M_T(Q, X, \omega) \approx \exp\left[(2.1\, X)^{5/3}\, N(Q, X)\, \omega^2\right], \tag{12}$$

where $M_T(Q, X, \omega)$ was given by the integral relation (equation 49 of Tofsted (1)),

$$M_T(Q,\, X,\, \omega) = \frac{4}{\pi} \int \mathrm{d}\boldsymbol{u}\, \frac{W_1(\boldsymbol{u} - \boldsymbol{\omega})\, W_1(\boldsymbol{u})}{M_0(\omega)}\, \exp\left\{ + F(D,\, \boldsymbol{u},\, \boldsymbol{\omega}) \right\}, \tag{13}$$

$$
\begin{aligned}
F(D,\, \boldsymbol{u},\, \boldsymbol{\omega}) \;=\; &\frac{32}{\pi} \int \mathrm{d}\boldsymbol{u}_a\, W_1(\boldsymbol{u}_a)\, [\boldsymbol{u}_a \cdot \boldsymbol{\omega}] \\
&\times \left(+ \mathcal{D}_\phi[D\,(\boldsymbol{u} - \boldsymbol{u}_a - \boldsymbol{\omega})] - \mathcal{D}_\phi[D\,(\boldsymbol{u} - \boldsymbol{u}_a)] \right).
\end{aligned}
\tag{14}
$$

Due to circular symmetry, M_T only depends on the magnitude $\omega = |\boldsymbol{\omega}|$. That is, one may always orient $\boldsymbol{\omega}$ along the x-axis without loss of generality.

In the prequel, based on the model given by equation 12, and based on figure 3 of Tofsted (1) that appeared to show ω^2 dependence of the exponent, it was believed to be unnecessary to evaluate equation 13 at every value of ω in order to evaluate a single point $V(Q, X)$. Rather, a single evaluation of $M_T(Q, X, \omega)$ could be performed for each Q and X combination, at a "characteristic" value of ω, call it ω_K. $N(Q, X)$ could then be evaluated for this computed M_T using the equation 12 model and the value of ω_K. The value of ω_K was chosen so that it would have the greatest impact on the overall curve, and thus the point $M_S(\omega_K) = 1/2$ was selected to model the behavior in the immediate vicinity of the knee of the complete MTF curve.

This choice, it turns out, had one useful feature, and one detrimental feature. The useful feature is that while (as I will show) we must abandon the previous model in general, as an approximation it is actually rather good. When compared with the newer model described further along in the current paper, it exhibits only a third of the error of the original Fried equation. The detrimental feature is that as the X parameter increases, the knee of the M_S curve falls at ever smaller values of ω. Thus the evaluation point is at smaller ω, and if (as we shall find) the N function is a varying function of ω, then the correlation between ω_K and X may produce unusual effects.

A further reason for restricting the computations to an evaluation at ω_K was a numerical precision issue with evaluating equation 14 and its effect upon introducing this result in the exponential argument in equation 13. The phase structure function is modeled as,

$$\mathcal{D}_\phi(D\, u) = 2\,(2.1\, X)^{5/3}\, u^{5/3}\, \alpha(Q\, u), \tag{15}$$

where $\alpha(Q\,u)$ is a diffraction related function that varies smoothly between 1/2 and 1 over an 8-decade range of its argument (see Tofsted (1)). However, the $X^{5/3}$ factor can produce exponential arguments exceeding 10^5 in equation 13. In the prequel the integration process was handled on-the-fly, which we found to be computationally intensive. To resolve the question of how N varies as $N(Q, X, \omega)$, this integration routine was completely reworked, as described in section 2. Then, in section 3 the updated $V(Q, X, \omega)$ function is considered, and its behavior is modeled in an approximate analytical form, as previously, but now as a function of three variables. The resulting behavior of the new functional form is considered in section 4.

2. Revised Integration Technique

To explore the variations of $V(Q, X, \omega)$ across the effective spectrum of Q, X, and ω we consider Q values extending from 1/16th through 16 by factors of 2 (9 points), X from 0.1 to 10^3 in steps of 1/10th of a decade (41 points), and ω from 0.01 through 0.99 plus a few extra points at small ω (103 points). In sum, the required number of calculated points increased by a factor of over 100. Hence, a new integration technique was needed that was both faster and more accurate.

The main problem, of course, was the factor $(2.1\,X)^{5/3} = S^{5/3}$ in $\mathcal{D}_\phi$ inside the F double integral of equation 14. To deal with this situation, let us first rewrite equation 15 as,

$$\mathcal{D}_\phi(D\,u) = 2\,(2.1\,X/Q)^{5/3}\,\varphi(Qu), \tag{16}$$

where,

$$\varphi(x) = x^{5/3}\,\alpha(x). \tag{17}$$

Using this functional form for the phase structure function, equation 14 can be rewritten,

$$
\begin{aligned}
F(D,\,\boldsymbol{u},\,\boldsymbol{\omega}) &= \frac{32}{\pi}\int \mathrm{d}\boldsymbol{u}_a\, W_1(\boldsymbol{u}_a)\,[\boldsymbol{u}_a \cdot \boldsymbol{\omega}] \\
&\quad \times (+\mathcal{D}_\phi[D\,(\boldsymbol{u}-\boldsymbol{u}_a-\boldsymbol{\omega})] - \mathcal{D}_\phi[D\,(\boldsymbol{u}-\boldsymbol{u}_a)]) \\
&= \frac{64}{\pi}(2.1\,X/Q)^{5/3}\int \mathrm{d}\boldsymbol{u}_a\, W_1(\boldsymbol{u}_a)\,[\boldsymbol{u}_a \cdot \boldsymbol{\omega}] \\
&\quad \times (+\varphi[Q\,(\boldsymbol{u}-\boldsymbol{u}_a-\boldsymbol{\omega})] - \varphi[Q\,(\boldsymbol{u}-\boldsymbol{u}_a)]) \\
&= (2.1\,X)^{5/3}\,\widetilde{F}(Q,\,\boldsymbol{u},\,\omega\,\widehat{\boldsymbol{x}}). \tag{18}
\end{aligned}
$$

This first step allows us to factor out $(2.1\,X)^{5/3}$ from the inner double integral. The function $\widetilde{F}$ can then be tabulated for $|\boldsymbol{u}| < 1/2$, $0 < \omega < 1$ (where radial symmetry always permits us to

orient $\boldsymbol{\omega}$ along the $+x$ axis), and Q, thereby reducing the problem of evaluating equation 13 from a four-dimensional integral to a two-dimensional integral plus an interpolation on a multi-dimensional look-up table of $\widetilde{F}(...)$ results. This greatly increases the calculation speed.

The remaining major problem due to the $X^{5/3}$ factor is solved by the addition of an iterative step during the computation of the outer double integral. The problem is that the M_T integral must be computed with $(2.1\,X)^{5/3}\,\widetilde{F}(...)$ inside the exponential factor. And while $\widetilde{F}$ evaluates to a quantity less than 10, the $X^{5/3}$ factor can be up to 10^5. And yet, once M_T is evaluated, the function N is evaluated by taking the log of M_T and dividing out the same $X^{5/3}$ factor:

$$N(Q,\,X,\,\omega) = \frac{\ln\left[M_T(Q,\,X,\,\omega)\right]}{(2.1\,X)^{5/3}\,\omega^2}. \tag{19}$$

Thus the $(2.1\,X)^{5/3}$ factor appears to cancel, but cannot simply be removed from the outer double integral prior to actually evaluating M_T. Nevertheless, one can write the M_T integral in the form,

$$\begin{aligned} M_T(Q,\,X,\,\omega) &= \frac{4\,\exp(+A)}{\pi}\int d\boldsymbol{u}\,\frac{W_1(\boldsymbol{u}-\boldsymbol{\omega})\,W_1(\boldsymbol{u})}{M_0(\omega)}\exp\left\{+F(D,\,\boldsymbol{u},\,\boldsymbol{\omega})-A\right\} \\ &= M_U(Q,\,X,\,\omega)\,\exp(+A), \end{aligned} \tag{20}$$

such that,

$$N(Q,\,X,\,\omega) = \frac{\ln\left[M_U(Q,\,X,\,\omega)\right]+A}{(2.1\,X)^{5/3}\,\omega^2}, \tag{21}$$

where a constant such as $\exp(+A)$ may always be both multiplied and divided from a quantity. This is necessary because the resolution limit of double precision does not extend to $\exp(10^5)$, yet a priori we do not know how much to initially subtract inside the exponent. And when we actually try to evaluate the result numerically, due to the double precision limitation we only know that the result has gone out of its proper bounds, but not by how much. We must therefore follow an iterative procedure to find an appropriate offset. Thus we initially set $A = 0$ and attempt the numerical computation. Each time the algorithm produces an out-of-bounds result, A is incremented by +40, and the numerical integration routine is run again. The integration is repeated, adjusting A, until such point that A is adjusted so that the numerical integration result produces a meaningful answer in the double precision logic of the routine.

Given both the tabulated and interpolated inner integral approach, along with the outer integral adjusted by the offset A, a complete set of $V(Q, X, \omega)$ values could be computed. Results were computed over the ranges of Q, X, and ω variations indicated at the beginning of this section. This range of the parameters covers the majority of the dynamic range of variations for most propagation conditions and optical systems used in terrestrial imaging scenarios.

6

Figure 2 illustrates the two extremes of the data set by plotting two sets of results for different x values as functions of ω for $Q = 1/16$ and 16. (Only half the curves are labeled.) From these curves, the values of $V(Q, X, 0)$ appear to be a function of Q alone. And apparently $V(Q, X, 1) \approx V(Q, X, 0)$ to within the level of accuracy of the calculations. Also, families of curves developed for different Q values exhibit similar features, indicating that further analysis (in the following section) may be capable of modeling this behavior using fewer than the 38,007 elements in the calculated sample database. The result of said analysis is a fitting function using a series of equations that produces estimates of $V(Q, X, \omega)$ that are virtually identical to the computed results.
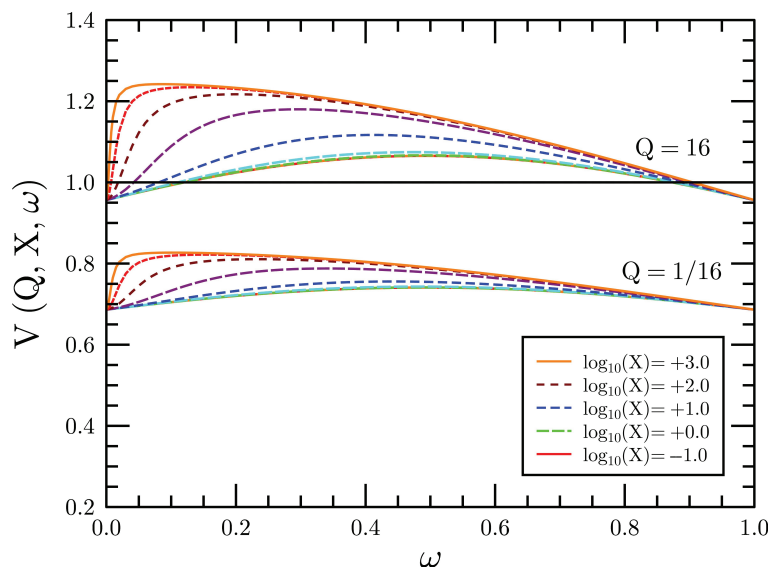

Figure 2. Plots of $V(Q, X, \omega)$ for $q = \log_2(Q) = +4$ and -4.

These results can be compared with the behavior of the previous analysis results seen in figure 1. A critical difference is that unlike the previous analysis, $V(Q, X, \omega)$ does not degrade with increasing X as did $V(Q, X)$. The reason the previous analysis showed decreasing $V(Q, X)$ with increasing X was because the evaluation point, ω_K, was a decreasing function of X.

3.   Analysis of $V(Q, X, \omega)$ Parameterization

The analysis process whereby the $V(Q, X, \omega)$ dependence was determined involved a lengthy sequence of analytical results to unpack the general behavior of the function into a sequence of similar behaviors. The first stage of this reduction involved the division of the function into two

segments: the base segment, designated V_0, apparently a function of only Q, and V_Δ, a variable portion dependent on Q, X, and ω:

$$V(Q, X, \omega) = V_0(Q) + V_\Delta(Q, X, \omega). \tag{22}$$

To model several of the resulting functions involved in characterizing these two constituent functions let us introduce a sigmoidal function,

$$\Sigma(x) = \frac{[\exp(x) - 1]}{[\exp(x) + 1]} = \frac{[\exp(+x/2) - \exp(-x/2)]}{[\exp(+x/2) + \exp(-x/2)]} = -\Sigma(-x). \tag{23}$$

We then employ a scaled and shifted form of this function:

$$S(x, A, B, C, D) = A + B\,\Sigma[C\,(x - D)]. \tag{24}$$

We shall also frequently need a spliced version of this function in which the exponential decays on either side of the $x = D$ center appear to exhibit different forms, designated,

$$S_S(x, A, B_1, B_2, C_1, C_2, D) = \begin{cases} A + B_1\,\Sigma[C_1\,(x - D)], & x \leq D; \\ A + B_2\,\Sigma[C_2\,(x - D)], & x \geq D. \end{cases} \tag{25}$$

Although this form is written with six free parameters, in actuality, to ensure continuity of the first derivate at the transition point, one degree of freedom is absorbed, whereby $B_1\,C_1 = B_2\,C_2$.

To model the baseline value we use,

$$V_0(Q) = S_S[\log_2(Q), 0.870, 0.370, 0.085, 0.355, 1.545, -1.00]. \tag{26}$$

Using this equation, the computed V results based on the integration technique described in the previous section were rendered into V_Δ by subtracting $V_0(Q)$. Next, it was recognized that the different families of V_Δ results could be better compared by normalizing each set of results at different Q values by dividing through by the maximum value of V_Δ in each subset. This maximum value invariably occurred at the maximum X value used ($X = 10^3$) at the peak point $\omega_P(Q, X)$. This maximum V_Δ (V_M) is given approximately by the relation,

$$V_M(Q) = S[\log_2(Q), 0.213, 0.072, 1.525, 0.150]. \tag{27}$$

Both $V_0(Q)$ and $V_M(Q)$ are plotted in figure 3 versus database derived results.
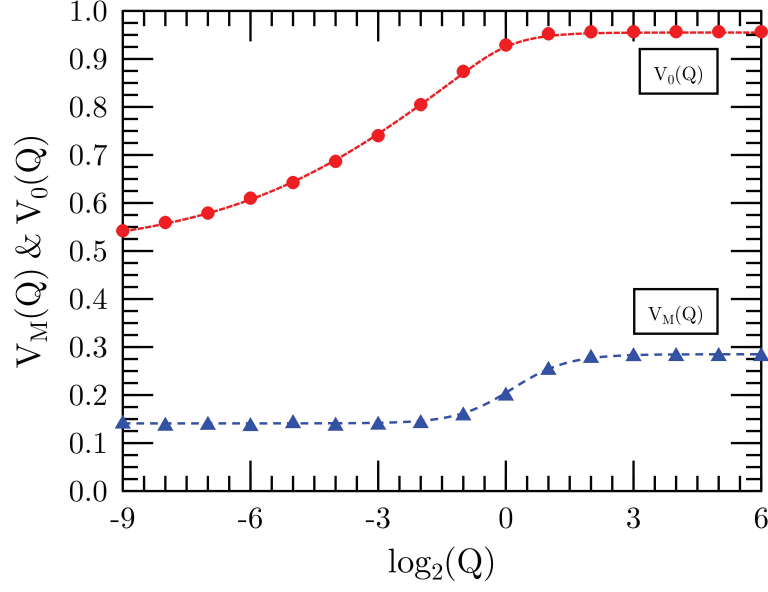
Figure 3. Plots of $V_0(Q)$ and $V_M(Q)$.

Division by $V_M(Q)$ produces sets of similar functions at each Q, $\widehat{V}_\Delta = V_\Delta/V_M$. Figures 4 and 5 compare two sets of such functions.
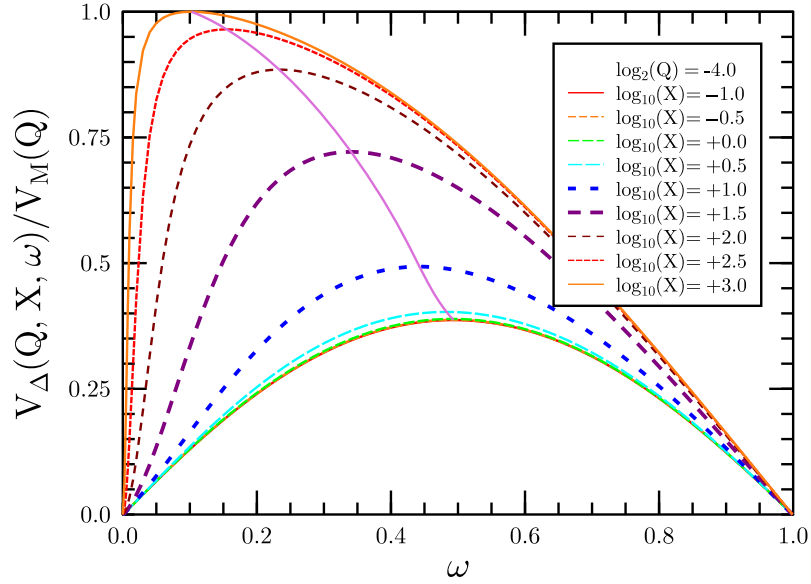

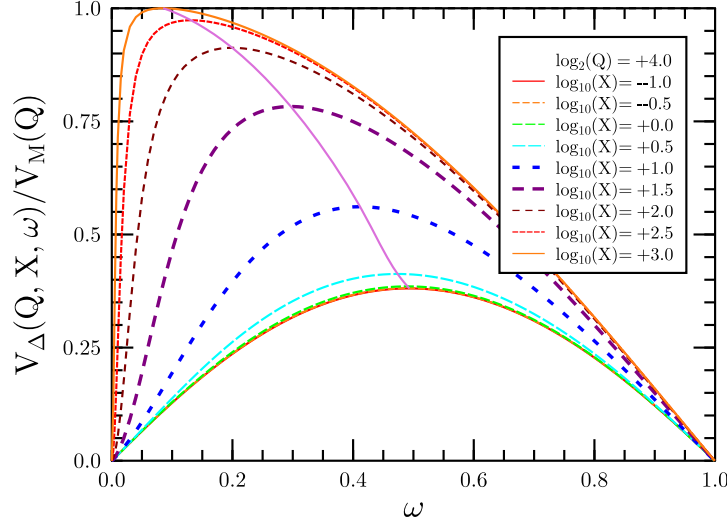Figure 4. Plots of $\widehat{V}_\Delta(Q, X, \omega)$ for Q=1/16.

Figure 5. Plots of $\widehat{V}_\Delta(Q, X, \omega)$ for Q=16.

Both plots illustrate sets of curves of similar shape. Both figures include a plot of the path corresponding to the position and height of the peak of each curve as a function of increasing X for that value of Q. Apparently the tracks of these peak curves are nearly identical, but different points along the paths are associated with different X values. As an illustration, figure 6 plots the ω components of these curves for various Q values as functions of $x = \log_{10}(X)$ [$\omega_P(Q, X)$].

To model the behavior of ω_P, the behavior of $\omega_P(Q = 1, X)$ may be used as the main guide function and shifted in $x = \log_{10}(X)$ by a function dependent on Q alone:

$$\omega_P(Q, X) = \omega_P[Q = 1, \ X/X_\omega(Q)]. \tag{28}$$

$$\omega_P(Q = 1, X) = S_S[\log_{10}(X), \ 0.360, \ -0.133, \ -0.322, \ 3.450, \ 1.424, \ 1.320]. \tag{29}$$

$$\log_{10}[X_\omega(Q)] = S[\log_2(Q), \ -0.004, \ 0.091, \ 1.750, \ -0.05]. \tag{30}$$

The resulting curve fit for $\omega_P(Q, X)$ is shown for the $Q = 1$ case in figure 7. Several shifted versions of other data sets based on the $X_s(Q)$ curve are also plotted.
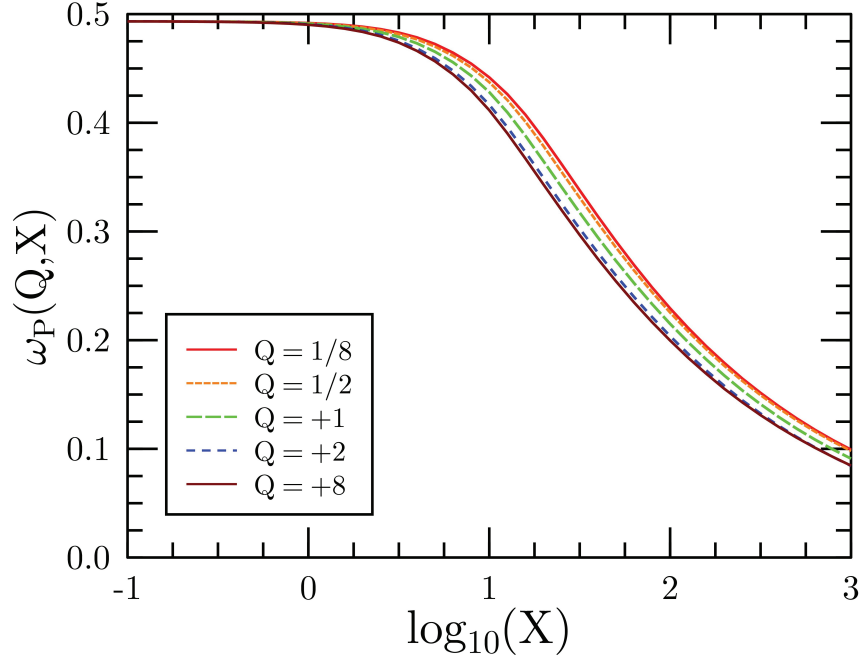
10

Figure 6. Plots of $\omega_P(Q, X)$ for various Q values.
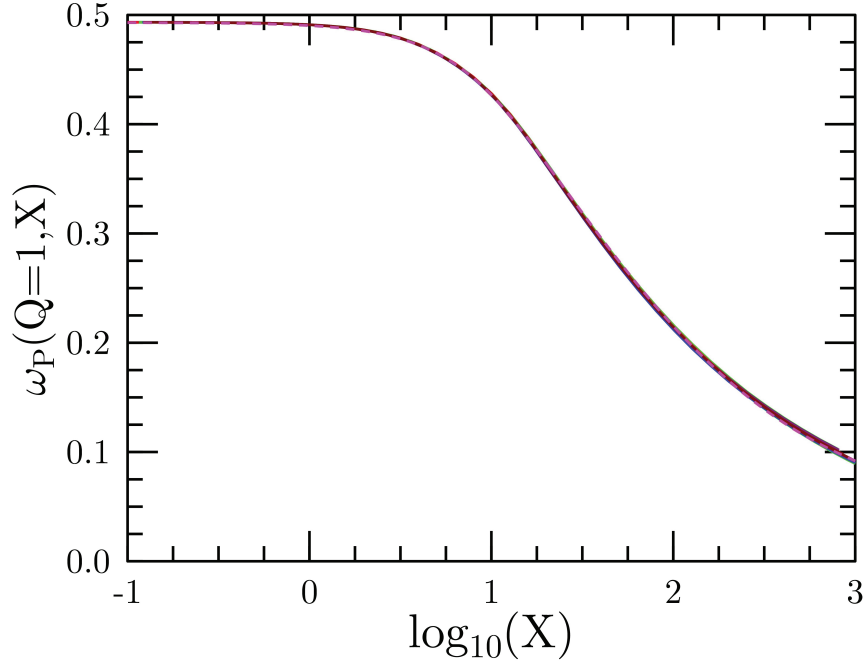
Figure 7. Plots of $\omega_P(Q = 1, X)$ for various x-shifted curves based on the $\omega_P(Q = 1, X)$ parametric curve.

Next, consider the vertical component of the peak curve. Define this function as $V_P(Q, X) = V_\Delta(Q, X, \omega_P)$. The behavior of $V_P(Q, X)$ is illustrated for several values of Q in figure 8. The salient features of these plots are that there is a similar shift in $x = \log_{10}(X)$ between the different curves along with a vertical scale factor.
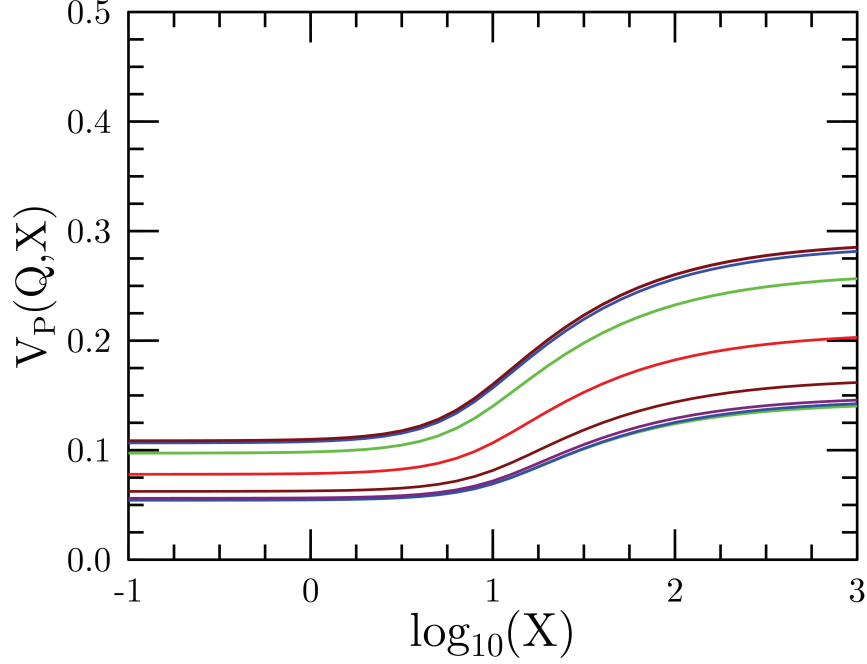
Figure 8. Plots of $V_P(Q, X)$ for various values of Q.

To model this behavior let us again characterize $V_P(Q, X)$ by first considering the peak function for $Q = 1$:

$$V_1(x) = V_P(Q = 1, x) = S_S(x, 0.122, 0.044, 0.082, 4.257, 2.300, 1.167). \tag{31}$$

Using this baseline function we rescale and shift it according to:

$$V_P(q, x) = A_R(q) V_1[x - x_P(q)], \quad q = \log_2(Q), \quad x = \log_{10}(X); \tag{32}$$

$$A_R(q) = S(q, +1.051, +0.3565, +1.600, +0.150); \tag{33}$$

$$x_P(q) = S(q, +0.005, -0.0880, +1.550, -0.150). \tag{34}$$

12

Given the peak value function, V_P, and the peak location, ω_P, one may then approximately model the functional dependence of $\widehat{V}(Q, X, \omega)$. However, the shape of the resulting function must still be parameterized by indexing this shape relative to the normalized peak value, $U_P(Q, X) = V_P(Q, X)/V_P(Q, 1000)$.

To model the shape of these functions, a scaled set of Legendre polynomial functions was employed. Let $P_0(u) = 1$, $P_1(u) = u$, and use equation 5.5.1 of Press et al. (5):

$$(n + 1)\, P_{n+1}(u) = (2n + 1)\, u\, P_n(u) - n\, P_{n-1}(u). \tag{35}$$

The u variable of Legendre polynomials ranges between -1 and +1, where it is evenly weighted. However, because $0 \leq \omega \leq 1$, we need to introduce new functions,

$$L_n(\omega) = \sqrt{2n + 1}\, P_n(2\,\omega - 1), \tag{36}$$

such that,

$$\int_0^1 L_m(\omega)\, L_n(\omega)\, \mathrm{d}\omega = \delta_{mn}, \tag{37}$$

expresses the orthonormal nature of the resulting rescaled functions.

In addition, the function expansion in weighted L_m functions may be reduced to fewer terms if the interval $(0...1)$ in ω is divided into two subsections $(0...\omega_P)$ and $(\omega_P...1)$. Then, the expansion of $\widehat{V}_\Delta(Q, X, \omega)$ may be expressed as,

$$
\begin{aligned}
\widehat{V}_\Delta(Q, X, \omega) &\approx \sum_{n=0}^{n=N} C_{2n}[U_P(Q, X)]\, L_{2n}\left\{ \frac{\omega}{2\,\omega_P(Q, X)} \right\}, \quad \omega \leq \omega_P; \\
\widehat{V}_\Delta(Q, X, \omega) &\approx \sum_{n=0}^{n=N} D_{2n}[U_P(Q, X)]\, L_{2n}\left\{ 1 - \frac{[1 - \omega]}{2\,[1 - \omega_P(Q, X)]} \right\}, \quad \omega \geq \omega_P.
\end{aligned}
\tag{38}
$$

This division is significant because only even order scaled-Legendre functions are needed, and also at $\omega \geq \omega_P$ fewer significant terms are needed. In particular, the series has been truncated at $N = 6$. The constants C_{2n} are then produced by integrating the scaled functions multiplied by each of the rescaled Legendre functions.

Though some scatter appears when performing these calculations, the similarities between the functions at different Q values are evident. These results are plotted in figures 9 and 10 for the C_{2n} and D_{2n} coefficients.
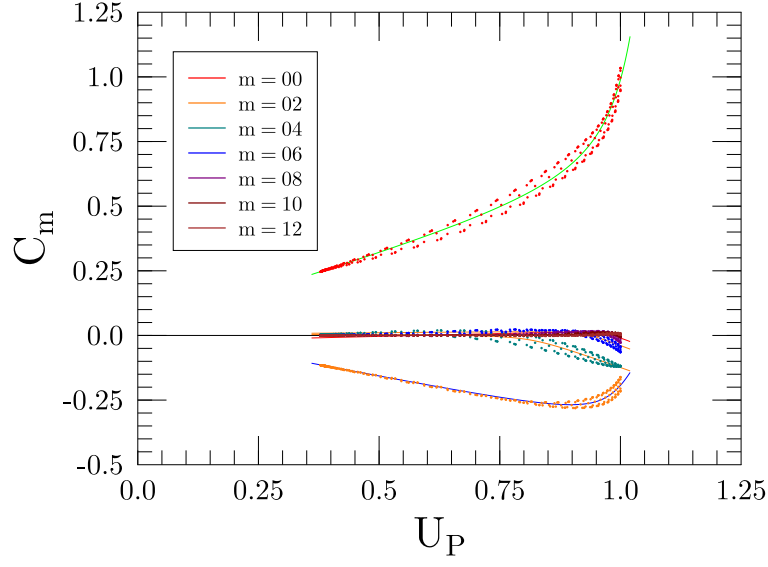
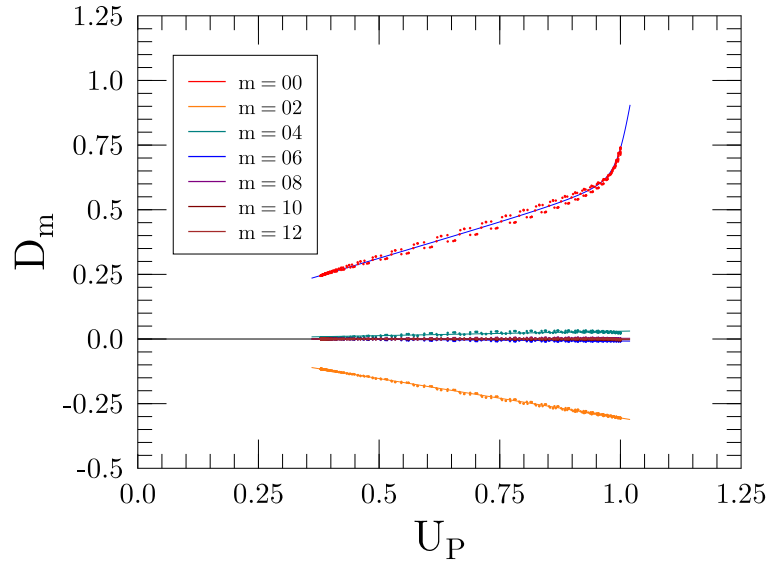Figure 9. Plots of $C_m = C_{2n}$ expansion coefficients and parametric curve fits to the results.

Figure 10. Plots of $D_m = D_{2n}$ expansion coefficients and parametric curve fits to the results.

For the C_{2n} plots, several coefficients appear to exhibit hyperbolic dependence, while of the D_{2n} coefficients only D_0 appears to exhibit hyperbolic behavior. These hyperbolic forms were modeled using the fitting function,

$$C_m = a_m \left(U_P - e_m \right) + b_m \sqrt{(U_P - e_m)^2 + c_m} + d_m. \tag{39}$$

The curves plotted in figures 9 and 10 are based on this equation. Coefficients used in these equations are detailed in tables 1 and 2. Table 1 details the coefficients associated with the hyperbolic cases. The remaining coefficients are considered linear in U_P, where the same model terms are used, but where constants b_m, c_m, and e_m are all set to zero.

Table 1. Hyperbolic Model C_m and D_m Coefficients.

Coefficient	a_m	b_m	c_m	d_m	e_m
C_0	20.1020	19.5598	0.0028	0.5700	1.0500
C_2	2.1140	2.4810	0.0041	-0.3503	0.9997
C_4	-0.3391	-0.3361	0.0050	0.0051	0.8141
C_6	-0.3533	-0.3721	0.0000	0.0131	0.9201
C_8	-0.3675	-0.3987	0.0001	0.0155	0.9632
D_0	6.4460	5.9010	0.0006	0.5810	0.9999

Table 2. Linear Model C_m and D_m Coefficients.

Coefficient	a_m	d_m
C_{10}	0.01013	-0.00448
C_{12}	0.00558	-0.00256
D_2	-0.30465	-0.00055
D_4	0.03405	-0.00396
D_6	-0.01269	0.00486
D_8	0.00429	-0.00153
D_{10}	-0.00444	0.00191
D_{12}	0.00055	-0.00016

The root mean square (RMS) error resulting from the use of these coefficients for V results computed at 9 Q values, 41 X values, and 105 ω values was 0.006795. This result was further improved by passing the resulting model into an algorithm utilizing a Stochastic Parallel Gradient

15

Descent (SPGD) approach of Vorontsov and Sivokon (6). The result of running this algorithm tended to optimize the coefficients, reducing the overall RMS error described above to 0.002728. Based on these results we must redefine the various equations previously presented. These are expressed using,

$$V_0(Q) = S_S[\log_2(Q), 0.8785, 0.3726, 0.0849, 0.3733, 1.5700, -0.9844]; \qquad (40)$$

$$V_M(Q) = S[\log_2(Q), 0.2205, 0.0696, 1.5387, 0.1502]; \qquad (41)$$

$$\omega_P(Q = 1, X) = S_S[\log_{10}(X), 0.3506, -0.1332, -0.3177, 3.4505, 1.4065, 1.2738]; \qquad (42)$$

$$\log_{10}[X_\omega(Q)] = S[\log_2(Q), 0.0040, -0.0877, 1.7450, -0.0502]; \qquad (43)$$

$$V_1(x) = V_P(Q = 1, x) = S_S(x, 0.1216, 0.0438, 0.0823, 4.2957, 2.3225, 1.1787); \qquad (44)$$

$$A_R(q) = S(q, +1.0657, +0.3521, +1.5964, +0.1498); \qquad (45)$$

$$x_P(q) = S(q, -0.0050, +0.0893, +1.5499, -0.1500). \qquad (46)$$

With these changes, the results in tables 1 and 2 are replaced by the coefficients of tables 3 and 4. The primary difference between these coefficients and the original parameter values appears to be due to the restrictions on the range of the Q and X parameters to the intervals 1/16 – 16 and 0.1 – 10^3, respectively. The SPGD method appears quite capable of optimizing the fitting properties if presented with a coefficient set that is fairly close to the optimal settings. On the other hand, if the SPGD method is supplied with an initial coefficient set that is initially a rather poor fit to the available data, then SPGD does very poorly in improving the fit to the data.

Table 3. SPGD Modified Hyperbolic Model C_m and D_m Coefficients.

Coefficient	a_m	b_m	c_m	d_m	e_m
C_0	20.2124	19.6324	0.0031	0.5751	1.0686
C_2	2.1118	2.4928	0.0042	-0.3515	0.9808
C_4	-0.3413	-0.3355	0.0051	0.0051	0.7996
C_6	-0.3529	-0.3769	0.0000	0.0131	0.9041
C_8	-0.3696	-0.3982	0.0000	0.0153	0.9504
D_0	6.4372	5.8919	0.0005	0.5788	1.0341

Table 4. SPGD Modified Linear
Model C_m and D_m
Coefficients.

Coefficient	a_m	d_m
C_{10}	0.01009	-0.00452
C_{12}	0.00550	-0.00257
D_2	-0.30273	-0.00057
D_4	0.03335	-0.00413
D_6	-0.01271	0.00485
D_8	0.00425	-0.00154
D_{10}	-0.00452	0.00186
D_{12}	0.00055	-0.00019

4. Results

The new model of $V(Q, X, \omega)$ allows us to compare the new results with the previous model
results. Perhaps the most telling examples are comparisons of the same cases presented in
figure 6 of Tofsted (*1*), reproduced here as figure 11. The new results are plotted in figure 12
below. In the prequel, several cases showed "super-resolution" characteristics by exceeding unity
at ω values greater than 0.7. The new curves never violate the diffraction limit, as argued by
Charnotskii (*4*), but also produce increased values in the functions at intermediate frequencies
$0.3 < \omega < 0.7$ because $V(Q, X, \omega)$ is larger at intermediate ω values than it is at the knee of the
curves.

The difference between the prequel paper's super-resolution results and the diffraction limited
results obtained here are also illustrated in figure 13 for a presumed worst case fit of the previous
analysis. That scenario is $Q = 4$ and $X = 2$. This combination produced $M_{SA}(\omega) > 1.25$ at
$\omega > 0.95$ in the previous analysis. As the figure shows, the prequel's $V = 1.0395$ produces a
function closer to the true MTF than the $\alpha = 1.0$ Fried case up until $\omega = 0.8$. The new function
is virtually identical to the calculated curve. Hence, the prequel's functional form still provides a
useful approximation, even though it violates the diffraction limit at extremely high frequency
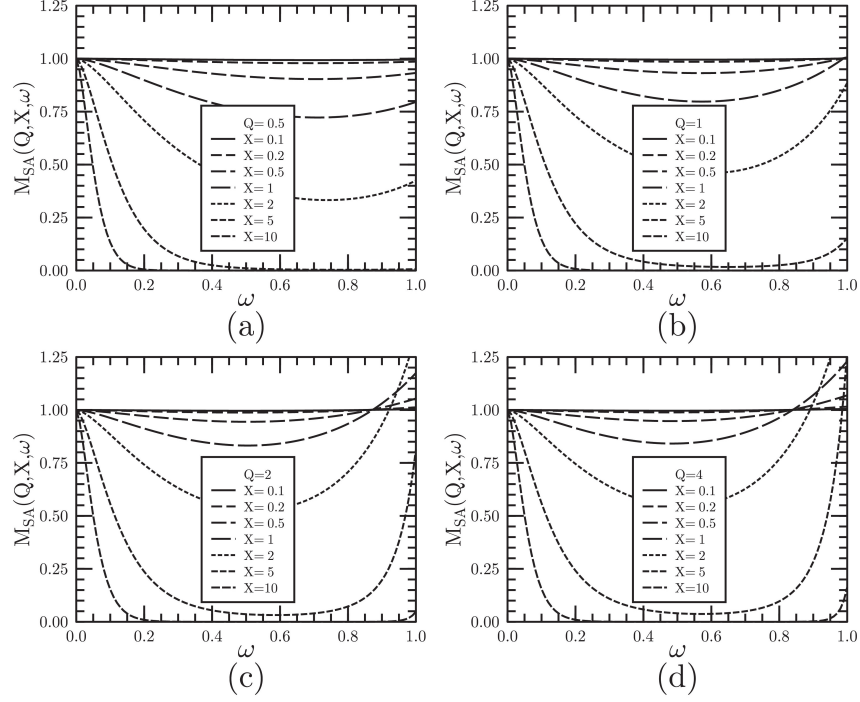($\omega > 0.87$).

Figure 11.   Atmospheric MTF's plotted for Q cases (a) 1/2, (b) 1, (c) 2, and
(d) 4, respectively, from the prequel paper where
super-resolution conditions were predicted where results
exceeded 1.0.

The various models can be compared against the complete set of short-exposure computed MTF values, i.e., the calculated $V(Q, X, \omega)$ data set. To produce a weighted sum squared error, the sum of the weighted squared difference between an estimate and the computed result, $\omega \, \delta M^2$, can be compared for five different methods of estimating the MTF. These estimation techniques are: (1) Fried's far-field case ($\alpha = 1/2$), (2) Fried's near-field case ($\alpha = 1$), (3) a Fried best-fit case (based on either $\alpha = 1/2$ or 1, depending on which case best fits the data), (4) the prequel's analytical model $V(Q, X)$, and (5) the current paper's extended analytical $V(Q, X, \omega)$ model. For each case the error between the computed MTF and the estimated result is computed (call it δM). The root mean squared error was then normalized according to,

$$R_C = \sqrt{\sum_i \delta M_i^2 \, \omega_i \, \Delta\omega_i / \sum_i \omega_i \, \Delta\omega_i}, \tag{47}$$

where C is the case number. The resulting five cases produced RMS errors $N_1 = 0.01409$, $N_2 = 0.03518$, $N_3 = 0.01079$, $N_4 = 0.00643$, and $N_5 = 0.00022$. Clearly the worst case is the Fried $\alpha = 1/2$ far-field case. Of course, the cases studied focused on the transition range from small to large Q values. If Q were extremely small, the $\alpha = 1/2$ case might be the best choice.
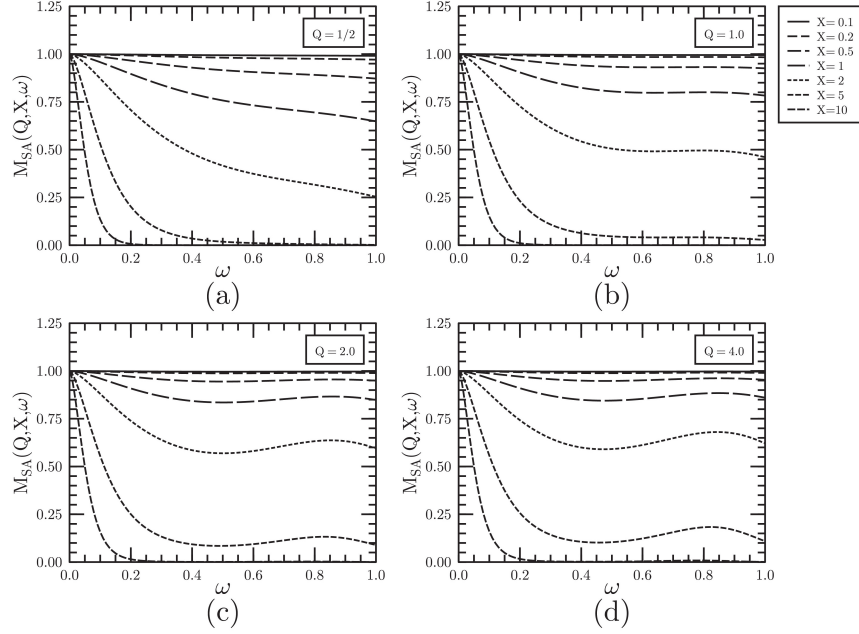
18

Figure 12. Atmospheric MTF's plotted for Q cases (a) 1/2, (b) 1, (c) 2, and (d) 4, respectively. Super-resolution cases of the prequel model are eliminated due to high frequency decay.

However, even when permitting a choice between the near-field and far-field cases, the Fried model exhibits significantly greater error than the case 4 results using the prequel's $V(Q, X)$ function. And of course, the case 5 model is obviously virtually equivalent to the full multi-dimensional integral of equations 13 and 14, being ~ 30 times better than the prequel's performance.

5. Conclusions

The analysis performed in this paper completes a research arc beginning nearly a decade ago with the publication of Tofsted (*7*). For many years researchers (c.f., MacDonald and Cain (*8*), and Dunphy and Kerr (*9*)) have alluded to weaknesses in Fried's (*2*) short-exposure model. The path of this arc led through Tofsted (*1*) which highlighted the missing term in Fried's approach. This paper completes the arc, following Charnotskii's (*4*) observation that the theory cannot support super-resolution, and resulted in a new understanding of the angular frequency in the V function. As before, an analytical expression was derived to describe the new dependence, though involving considerably more detail. In the process the degree of accuracy of the new method was
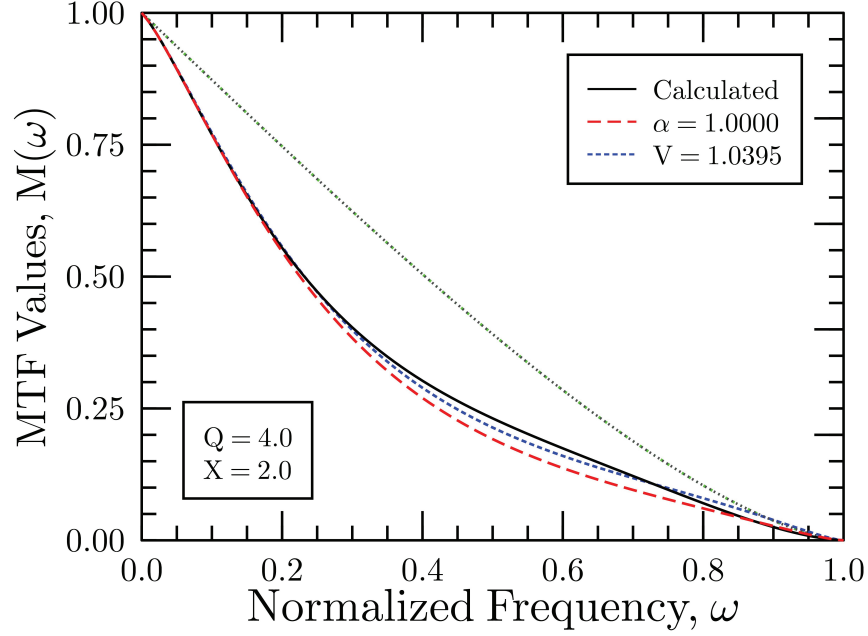
Figure 13. Atmospheric MTF's plotted for Q=4 and X=2 comparing Fried's model (red dashed) for <alpha>=1, Tofsted approximate model (blue dashed) for V=1.0395, and full model (black solid) results, along with system MTF (dashed green) curve..

compared, along with the prequel version and Fried's original analysis with the more extensive calculations, revealing that the new method has virtually no error, while the prequel method has one-third the error of Fried's original method using $\alpha = 1$.

These new results can also be directly coupled to the results of a recent paper (*10*) that studied the influence of path-varying turbulence strength for two classes of path geometry: slant path over flat terrain and flat path over valley terrain. In both cases it was found that changes in the behavior of the wave and phase structure functions with path varying turbulence could be parameterized through scaling functions based on path geometry to modify the X and Q parameters of these structure functions. Since the results of this paper continue to use the same structure functions, the same techniques may be applied to adjust the X and Q parameters of the new MTF model to account for path-varying turbulence.

The key missing element of the current and previous studies has been and is the lack of consideration of inner scale influences on the structure functions. However, since the focus of these studies has been the impacts of turbulence on aided optical systems, in most cases inner scale effects are minor. In contrast, outer scale effects may be significant on the angle-of-arrival variance, but only for larger aperture optics. For systems considered here that are less than

10-inches in aperture diameter, the effects of outer scale on angle-of-arrival variance will be less than 10% (see e.g., Tofsted (*10*), which is typically less (under most conditions) than the uncertainty in the measurement of C_n^2 itself.

6. References

1. Tofsted, D. H. Reanalysis of Turbulence Effects on Short-exposure Passive Imaging. *Opt. Eng.* **2011**, *50*, 016001.

2. Fried, D. L. Optical Resolution Through a Randomly Inhomogeneous Medium for Very Long and Very Short Exposures. *J. Opt. Soc. Am.* **1966** *56*, 1372–1379.

3. Goodman, J. W. *Statistical Optics*; J. Wiley & Sons, 1985.

4. Charnotskii, M. Statistics of the Point Spread Function for imaging through turbulence. *Proc. SPIE 8014-30*, 2011.

5. Press, W. H.; Teukolsky, S. A.; Vetterling, W. T.; Flannery, B. P. *Numerical Recipes in C*; Cambridge Univ. Press, 1992.

6. Vorontsov, M. A.; Sivokon, V. P. Stochastic Parallel Gradient Descent Technique for High-resolution Wave-front Phase-distortion Correction. *J. Opt. Soc. Am. A* **1998**, *15*, 2745–2758.

7. Tofsted, D. H. Analytic Improvements to the Atmospheric Turbulence Optical Transfer Function. *Proc. SPIE* **2003**, *5075*, 281–292.

8. MacDonald, A.; Cain, S. C. Parameterized Blind Deconvolution of Laser Radar Imagery Using an Anisoplanatic Optical Transfer Function. *Opt. Eng.* **2006**, *45*, 116001.

9. Dunphy, J. R.; Kerr, J. R. Turbulence Effects on Target Illumination by Laser Sources: Phenomenological Analysis and Experimental Results. *Appl. Opt.* **1977**, *16*, 1345–1358.

10. Tofsted, D. H. Short-Exposure Passive Imaging Through Path-Varying Convective Boundary Layer Turbulence. *Proc. SPIE* **2012**, *8355*, 83550J-1-12.

NO. OF COPIES	ORGANIZATION
1 ELEC	ADMNSTR DEFNS TECHL INFO CTR ATTN DTIC OCP 8725 JOHN J KINGMAN RD STE 0944 FT BELVOIR VA 22060-6218
1 CD	US ARMY NIGHT VISION & ELECTRONICS SENSORS DIRECTORATE SENSOR PERFORMANCE BRANCH ATTN AMSRD CER NV MS SP R ESPINOLA 10221 BURBECK RD FT BELVOIR VA 22060-5806
1 CD	STARFIRE OPTICAL RANGE ATTN AFRL RDS T FARRELL KIRTLAND AFB ALBUQUERQUE NM 87117
1 CD	DRDC VALCARTIER ATTN G POTVIN 3701 CARLING AVE OTTAWA ONTARIO K1A 0Z4 CANADA
1 CD	US ARMY RSRCH LAB ATTN RDRL CIE D R BRICE WHITE SANDS MISSILE RANGE NM 88002
1 CD	US ARMY RSRCH LAB ATTN RDRL CIE M R SHIRKEY BLDG 1622 WHITE SANDS MISSILE RANGE NM 88002
1 CD	US ARMY RSRCH LAB ATTN RDRL CIE D D HOOCK BATTLEFIELD ENVIR DIV BLDG 1622 WHITE SANDS MISSILE RANGE NM 88002-5001
2 CDS	US ARMY RSRCH LAB ATTN RDRL CIE D D TOFSTED WHITE SANDS MISSILE RANGE NM 88002-5501

NO. OF COPIES	ORGANIZATION
2 CDS	US ARMY RSRCH LAB ATTN RDRL CIE D M S DARCY ATTN RDRL CIE D S OBRIEN WHITE SANDS MISSILE RANGE NM 88002-5501
1 CD	US ARMY RSRCH LABORATORY ATTN RDRL CIE D E CREEGAN BLDG 1622, ROOM 201 WHITE SANDS MISSILE RANGE NM 88002
4 CDS	US ARMY RSRCH LAB ATTN IMAL HRA MAIL & RECORDS MGMT ATTN RDRL CIE D C KLIPP ATTN RDRL CIO LL TECHL LIB ATTN RDRL CIO LT TECHL PUB ADELPHI MD 20783-1197

TOTAL: 16 (1 PDF, 15 CDS)